J Oceanogr (2015) 71:361–372
DOI 10.1007/s10872-015-0295-3

ORIGINAL ARTICLE

Temporal variability of the current in the northeastern South China Sea revealed by 2.5-year-long moored observations

Li Cheng[1] · **Zhiwei Zhang**[1] · **Wei Zhao**[1] · **Jiwei Tian**[1]

Received: 1 September 2014 / Revised: 9 March 2015 / Accepted: 20 April 2015 / Published online: 29 April 2015

Abstract The current in the northeastern South China Sea (NSCS) has been extensively studied by both observations and numerical models, but its vertical structure and temporal variability are still not well understood because of the lack of long-term and full-depth direct observations. From August 2010 to March 2013, the current velocity in the NSCS was directly observed by Acoustic Doppler Current Profilers from a subsurface mooring at 117°52.07′E, 21°06.68′N. The observed current velocity was coherent in the vertical direction and nearly showed the same sign in the nearly full water column (960 m). The observed current presented strong intraseasonal variabilities (ISVs) within periods between 30 and 90 days. Analysis of the altimeter observation suggested that the ISVs were closely related to the propagating mesoscale eddies. Corresponding to the seasonally varying circulation in the NSCS, the ISV-removed current roughly showed a semiannual cycle. The seasonal U (V) averaged over 80–200 m depths reached the peak in March and October (January and July) and the trough in July and February (April and August), respectively, with a peak-to-trough amplitude of 0.14 m/s (0.19 m/s). Dynamical modes analysis suggested that the observed current velocity showed dominated energy in the barotropic mode during most of the observation period but enhanced energy in the first baroclinic mode during eddy events because of the enhanced vertical shear of velocity.

Keywords Northeastern South China Sea · Seasonal variabilities · Intraseasonal variabilities · Mesoscale eddies · Circulation

1 Introduction

The South China Sea (SCS) is the largest marginal sea in the northwestern Pacific, with a maximum depth of over 5000 m (Fig. 1). The surface wind over the SCS is dominated by the East Asia monsoon, northeasterly in winter and southwesterly in summer. Driven by the seasonally reversed monsoon, the upper SCS generally presents a basin-scale cyclonic circulation in winter and an anti-cyclonic circulation in the Southern SCS in summer (Wyrtki 1961; Liu and Xie 1999; Shaw et al. 1999; Morimoto et al. 2000; Hu et al. 2000; Qu 2000; Liu et al. 2008). Besides the seasonal time scale, the upper circulation of the SCS was also found to have prominent interannual variations, which were closely related to the interannual variations of the monsoon modulated by the El Niño/Southern Oscillation (Wu et al. 1998, Wu and Chang 2005; Shaw et al. 1999). In addition to the East Asian monsoon, the water exchange with the adjacent seas or open oceans can also have a significant impact on the SCS circulation (Lan et al. 2013; Chen and Xue. 2014). The Luzon Strait is a key channel connecting the SCS and the Pacific, through which the Kuroshio can occasionally intrude into the northeastern SCS (NSCS). The Kuroshio intrusion can bring a huge momentum and different water mass into the NSCS and thus can greatly influence the NSCS circulation (Wyrtki 1961; Shaw 1991; Qu 2000; Xue et al. 2004; Gan et al. 2006). Furthermore, based on an 8-month long direct current observation in the NSCS, Wang et al. (2013) studied the current deflection around Dongsha Islands.

✉ Jiwei Tian
tianjw@ouc.edu.cn

[1] Physical Oceanography Laboratory/Qingdao Collaborative Innovation Center of Marine Science and Technology, Ocean University of China, Qingdao, China

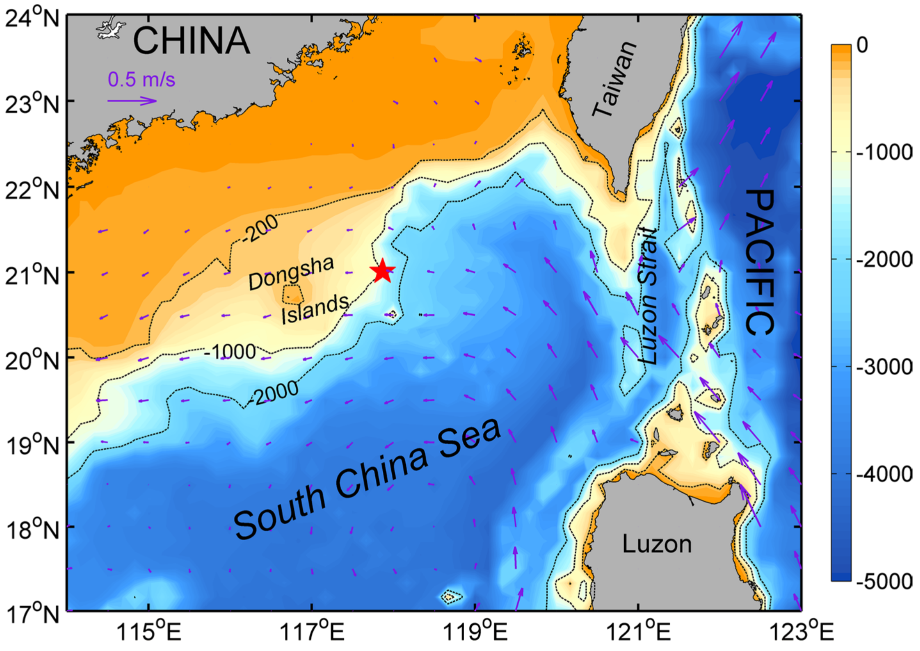

Fig. 1 Bathymetry of the NSCS and mooring location (*red pentagon*). The 200-, 1000- and 2000-m isobaths are marked with *dashed lines*. The *purple arrows* represent the climatological surface geostrophic currents diagnosed from the mean surface dynamic topography of Maximenko et al. (2009)

Beyond the seasonal and interannual time scales, both previous observation and modeling studies demonstrated that the upper SCS circulation also showed strong intraseasonal variability (ISV) (Wu et al. 2005; Wu and Chiang 2007; Zhuang et al. 2010). In the deep basin of the SCS, the ISV of circulation is largely caused by the mesoscale eddies generated by oceanic instabilities (Zhuang et al. 2010). Locally speaking, the ISV of observed current is closely related to the propagating mesoscale eddies (Wu and Chiang 2007). Interestingly, Zhang et al. (2013) even found that the deep current in the NSCS can be strongly modulated by the mesoscale eddies. They suggested that the mesoscale eddies are sometimes full-depth phenomena that can largely influence the deep circulation. The mesoscale eddies in the SCS have been intensively studied in recent years, through both satellite and in situ observations and numerical models (Wang et al. 2003, 2008a, b; Xiu et al. 2010; Chen et al. 2011; Nan et al. 2011a, b; Hu et al. 2011, 2012; Zhang et al. 2015). The statistics based on altimeter observation showed that the NSCS is a region of energetic eddy activities (Wang et al. 2003; Chen et al. 2011). The mesoscale eddies in the NSCS were generally generated southwest of Taiwan and northwest of Luzon; after generations, these eddies tended to propagate westward and southwestward (Wang et al. 2003; Chen et al. 2011).

Although the circulation in the NSCS and its temporal variabilities were extensively investigated by the previous studies, they were mainly based on satellite/hydrographic observations and numerical models. Due to the lack of direct current observations, especially full-depth and long-time moored observations, the vertical structure of the currents and its multi-scale temporal variabilities were still not well known. Based on 2.5-year-long direct current measurements collected from a subsurface mooring, the present study is intended to investigate the vertical structure and temporal variabilities of the current in the NSCS.

The rest of the article is organized as follows. Section 2 introduces the data we used. Section 3 shows the observed results, including the seasonal and intraseasonal variabilities of the current. Section 4 summarizes the study and gives some discussions.

2 Observations and data processing

2.1 Moored data

To monitor the current velocity in the northeastern SCS, a subsurface mooring was deployed at 117°52.07′E, 21°06.68′N (in Fig. 1), for about 2½ years from 23 August 2010 to 8 March 2013. The water depth of the mooring location is about 960 m. The mooring was deployed and recovered three times, and for each deployment the mooring setting was different. During the first (third) deployment, from 23 August 2010 (30 March 2012) to 18 April 2011 (8 March 2013), the mooring was equipped with an up-ward-looking 75-kHz ADCP (Acoustic Doppler Current Profilers) at 441 m (552 m) to measure the velocity on the upper 425 m (537 m). During the second deployment, from 27 April 2011 to 30 March 2012, two ADCPs, one looking upward and one downward, were moored at 478 m to cover the top 911-m water column. Table 1 shows detailed information about the mooring settings and the instrument parameters.

Table 1 Information on the moorings deployed in the NSCS

Observation period	Instrument (looking)	Instrument depth (m)	Range depth (m)	Sample interval (min)	Bin size (m)
23 Aug 2010–18 Apr 2011	ADCP (up)	441	36–425	3	8
27 Apr 2011–30 Mar 2012	ADCP (up)	478	41–465	5	8
	ADCP (dw)	478	495–911	5	8
30 Mar 2012–8 Mar 2013	ADCP (up)	552	49–537	3	8

ADCPs are 75-kHz Long Rangers manufactured by the TRDI Co. The 'up' and 'dw' indicate ADCPs looking upward and downward, respectively

Influenced by the tide and mesoscale eddies, the upper part of the moorings sometimes had large vertical excursions (~50 m). The swing of the mooring can cause a maximum of 1.5 cm/s velocity error in the uppermost layer; this velocity error is much smaller than the upper-layer velocity and thus would not substantially influence the conclusions of the present study. To get vertically gridded data, the velocity data were interpolated onto 5-m-interval levels according to the pressure records of ADCPs. Because the present study is focused on the low-frequency current, the current velocity was low-pass filtered with a cutoff period of 10 days to remove the tidal and inertial oscillations and other high-frequency signals. Finally, the velocity data were averaged on a daily basis. The following analysis in the present study was primarily based on this daily averaged zonal (*U* hereafter) and meridional velocity (*V* hereafter) data.

2.2 Altimeter data

To better understand the temporal variabilities of the NSCS circulation, we also utilized the weekly sea level anomaly (SLA) data and the absolute surface geostrophic velocity data (http://www.aviso.oceanobs.com/). Both the SLA and surface geostrophic velocity were on a gridded map and have a spatial resolution of 1/4° and 1/3°, respectively. This altimeter data set merges different altimeter observations including TOPEX/POSEIDON, Jason-1, ERS-1 and ERS-2. Compared to the older version, it has greatly improved the tidal and atmospheric barometric corrections and is more reliable in circulation studies. To be consistent with the moored velocity data, the above altimeter data were interpolated onto a daily resolution.

3 Results

The time-depth plots of the observed U and V are shown in Fig. 2. The most prominent feature visible is the large intraseasonal fluctuations. The strongest intraseasonal fluctuation occurred in January/February 2012, during which time the uppermost-layer velocity reached nearly 1 m/s. Although the velocity generally decreased with increasing depth, the ISVs signals were still evident near the water bottom (~900 m). The seasonal variability, on the other hand, can hardly be seen in Fig. 2 because of the contamination of strong ISVs. In order to investigate the seasonal variability of the observed current velocity, we needed to first remove the ISVs. The details of the seasonal variability and ISVs of the current will be further addressed in Sects. 3.1 and 3.2, respectively.

3.1 Seasonal variability

As revealed in Fig. 2, the *U* and *V* showed strong ISVs. To investigate the seasonal variability of the observed current, the ISVs were first removed using a low-passing filter with a cutoff period of 90 days. This cutoff period was chosen because that power spectrum of the observed velocity generally showed energy peaks in periods shorter than 90 days (Fig. 5b). We also used a 120-day low-pass filtering but found that the results did not change much. Because the observation depths were different in three observation periods, we only analyzed the results at the common depths in this section, i.e., between 80 and 420 m. The observation of the second deployment nearly covered the full water column. The seasonal-mean velocity profile during this observation period kept the same sign in the full water depth (not shown); therefore, we think that the seasonality revealed here can apply to the full water column.

To clearly show the seasonality of the *U*, *V* and absolute velocity, a monthly composite based on the 2.5-year time series was made (Fig. 3). The *U* averaged over 80–200-m depths displayed a roughly semiannual cycle, reaching the maximum in March (−11 cm/s) and October (−13.7 cm/s) and the minimum in July (0.2 cm/s) and February (−1.9 cm/s), respectively. The peak-to-trough amplitude of this semiannual cycle was 13.9 cm/s. Similar to the monthly *U*, the monthly *V* also showed a semiannual cycle. The difference is that the *V* reached the peak in January (13.4 cm/s) and July (2.9 cm/s) but the trough in April (−5.5 cm/s) and August (−4.2 cm/s). The amplitude of semiannual *V* was 18.9 cm/s, larger than that of *U*. Despite the seasonal variability, the monthly averaged *U* almost

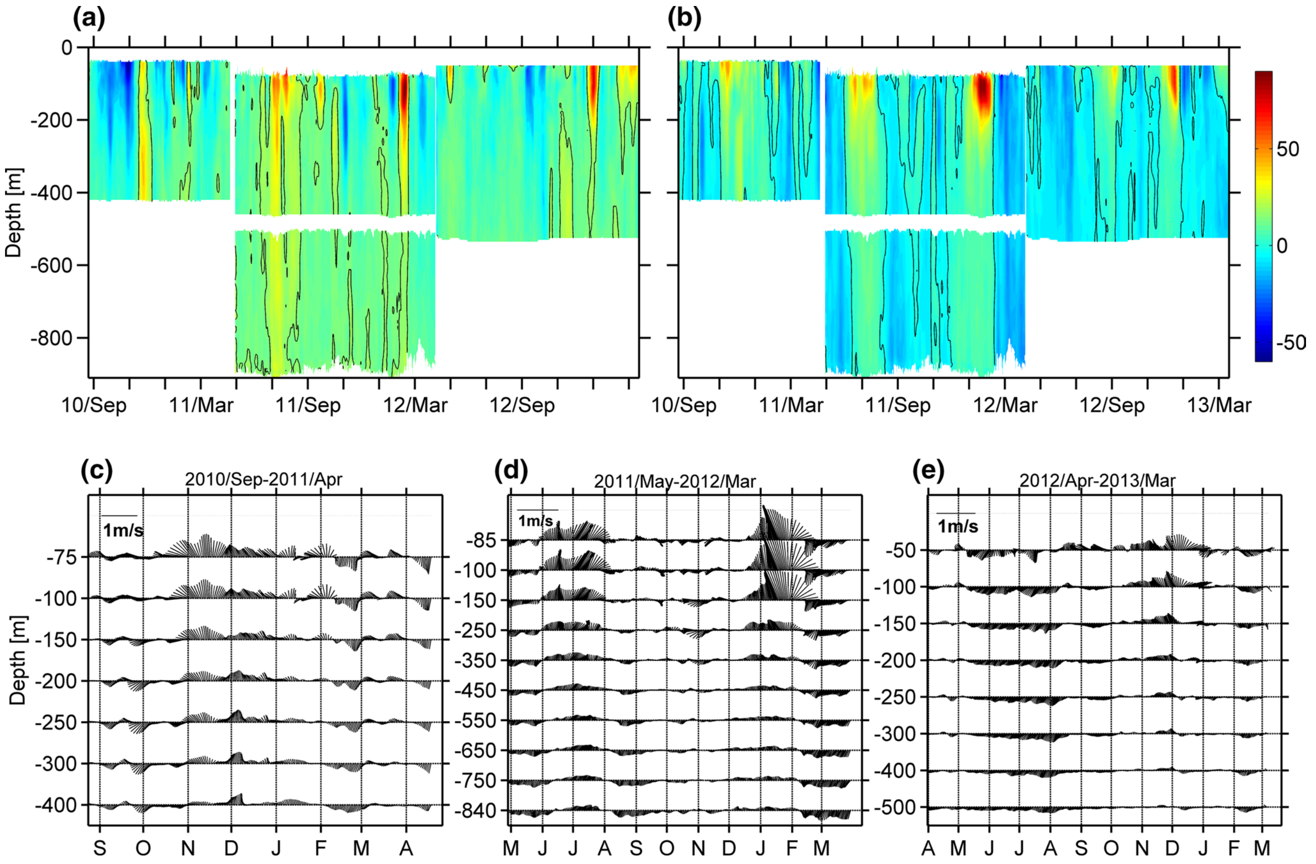

Fig. 2 **a** Time-depth plot of the observed *U*. The time series was low pass filtered for 10 days to remove the high-frequency fluctuations (such as tidal and inertial oscillations). The contour interval is 0.5 cm/s with the *black line* denoting the zero-velocity contour. *Panel* **b** is the same as *panel* **a**, but shows the results of the meridional velocity component. **c** *Stick plots* of the low-pass-filtered velocity at different depths in the first deployment. Note that the *y*-axis is not linear, and the *upward direction* of the *stick* represents the north. **d** and **e** are the same as **c**, but for the second and the third deployment, respectively

stayed uniformly in a westward direction in a year. The monthly *V*, on the other hand, showed various directions in different seasons. In correspondence with the *U* and *V*, the absolute velocity also displayed a semiannual cycle, reaching the maximum in March (12 cm/s) and October (13.9 cm/s) and the minimum in July (2.9 cm/s) and February (3.6 cm/s), respectively. The peak-to-trough amplitude of this semiannual cycle was 0.11 m/s. The monthly *U*, *V* and absolute velocity averaged over 200–420 m had similar features to the 80–200-m layer, only with reduced amplitudes.

Figure 4 presents the seasonal mean geostrophic current in the NSCS obtained from the altimeter data. For comparison, the mooring-observed seasonal mean velocity on the uppermost common depth (80 m) was also plotted (red arrow). Generally, the direction of mooring-observed velocity agreed well with the surface geostrophic current; the locally observed velocity changed corresponding to the seasonal NSCS circulation. In the winter and spring seasons, the NSCS was occupied by a cyclonic circulation pattern (Fig. 4a, d), which was part of the basin cyclonic gyre driven by the winter monsoon (Wyrtki 1961; Xu et al. 1982; Xue et al. 2004). A cyclonic circulation pattern still existed in autumn (Fig. 4c), but it became unclear in summer (Fig. 4b). In the region southwest of Taiwan, there was an anti-cyclonic mesoscale circulation in autumn and winter (Fig. 4c, d). This mesoscale circulation was indicative of the Kuroshio loop current, which usually occurrs in the winter seasons (Jia and Chassignet, 2011; Nan et al. 2011c). In the autumn and winter, the mooring site was under the influence of the west part of Kuroshio loop current; correspondingly, the mooring-observed current flowed northwestward. To examine the consistency between the mooring and altimeter velocity, we calculated their correlation coefficients at each layer (Fig. 4e, f). The mooring-observed *U* (*V*) was well correlated with the altimeter *U* (*V*), with the maximum correlation coefficient reaching 0.64 (0.65) on the uppermost layer (80 m); although the correlation coefficient gradually decreased with depth, it was still as high as 0.35 (0.51) at 420 m, which was

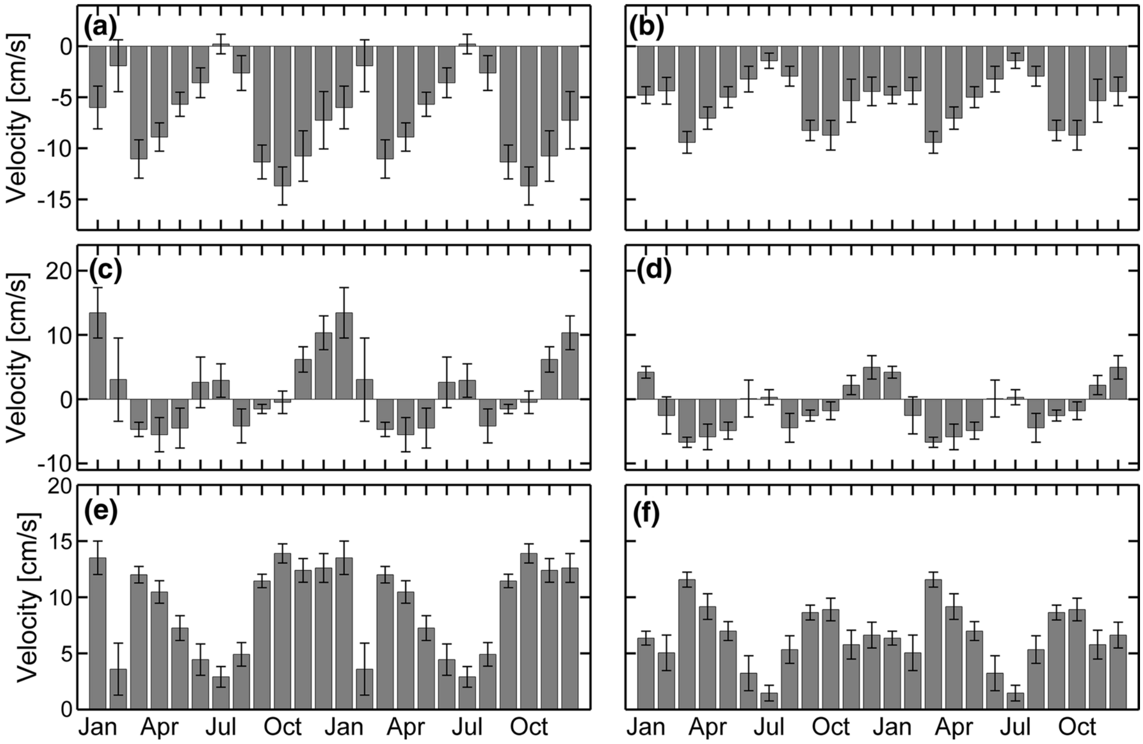

Fig. 3 Seasonal variations of U (**a**), V (**c**) and absolute velocity (**e**) averaged between 80 and 200 m (*gray bars*). The monthly mean value is calculated based on the velocity in every same month of the whole observation period. The *black thin bars* denote the standard deviations. In order to clearly show the seasonal cycle, the monthly U, V and absolute velocity were repeated twice. The *right panels* **b**, **d** and **f** are the same as **a**, **c** and **e**, respectively, except for the depth between 200 and 420 m. Before we computed the monthly mean velocity, the intraseasonal variability was first removed from the time series using 90-day low-pass filtering

significant above the 95 % confidence level. The good correlation between the mooring velocity and altimeter surface velocity suggested that the mooring-observed subtidal current was geostrophic to a large degree. It also demonstrated that the seasonal variability of the mooring-observed current corresponded to the seasonally varying circulation in the NSCS as revealed by the altimeter observation.

3.2 ISV

The time series of U averaged over 80–420 m is shown in Fig. 5a, from which strong ISVs can be found. The magnitude of the depth-averaged U can occasionally exceed 0.25 m/s. For example, the U reached -27.8 cm/s in late October 2011, then it sharply increased and became -14 cm/s about 24 days later; the U was -18 cm/s in mid January 2012 and sharply increased to 27.9 cm/s in early February 2012. In correspondence with the velocity, the kinetic energy (i.e., $(U^2 + V^2)/2$) also showed strong ISVs. The maximum kinetic energy occurred in mid January 2012 with the magnitude of 0.13 m^2/s^2. The power spectrum analysis showed that the depth-averaged U showed significant energy peaks in the band between 30 and 90 days (Fig. 5c). The power spectra of the zonal altimeter velocity displayed similar results except that it had stronger energy at around 60 days (Fig. 5d). The regions southwest of Taiwan and northwest of Luzon were revealed to have strong mesoscale eddy activities; after generation, these mesoscale eddies tend to propagate westward and southwestward (Wang et al. 2003; Chen et al. 2011) and thus can influence the mooring sites. The remainder of this section will investigate whether the propagating mesoscale eddies are the cause of the strong ISVs of the observed velocity. The vertical structure of the strong ISV events is also examined in this section.

To investigate whether the ISVs were associated with mesoscale eddies, we detected the eddies using the altimeter data. The method was primarily based on the algorithm used in Chen et al. (2011), and the readers can refer to their paper for details. Eventually, six long-lived eddies (with the lifespan larger than 4 weeks) were detected influencing the mooring site over 2.5 years, including two cyclonic eddies and four anti-cyclonic eddies. In chronological sequence, we called the two cyclones CA and CE and the four anti-cyclones WB, WC, WD and WF, respectively. Figure 6a shows the time series of SLA at the mooring site and the observed kinetic energy averaged over 80–420 m, with the detected eddies specified by gray strips. Comparing

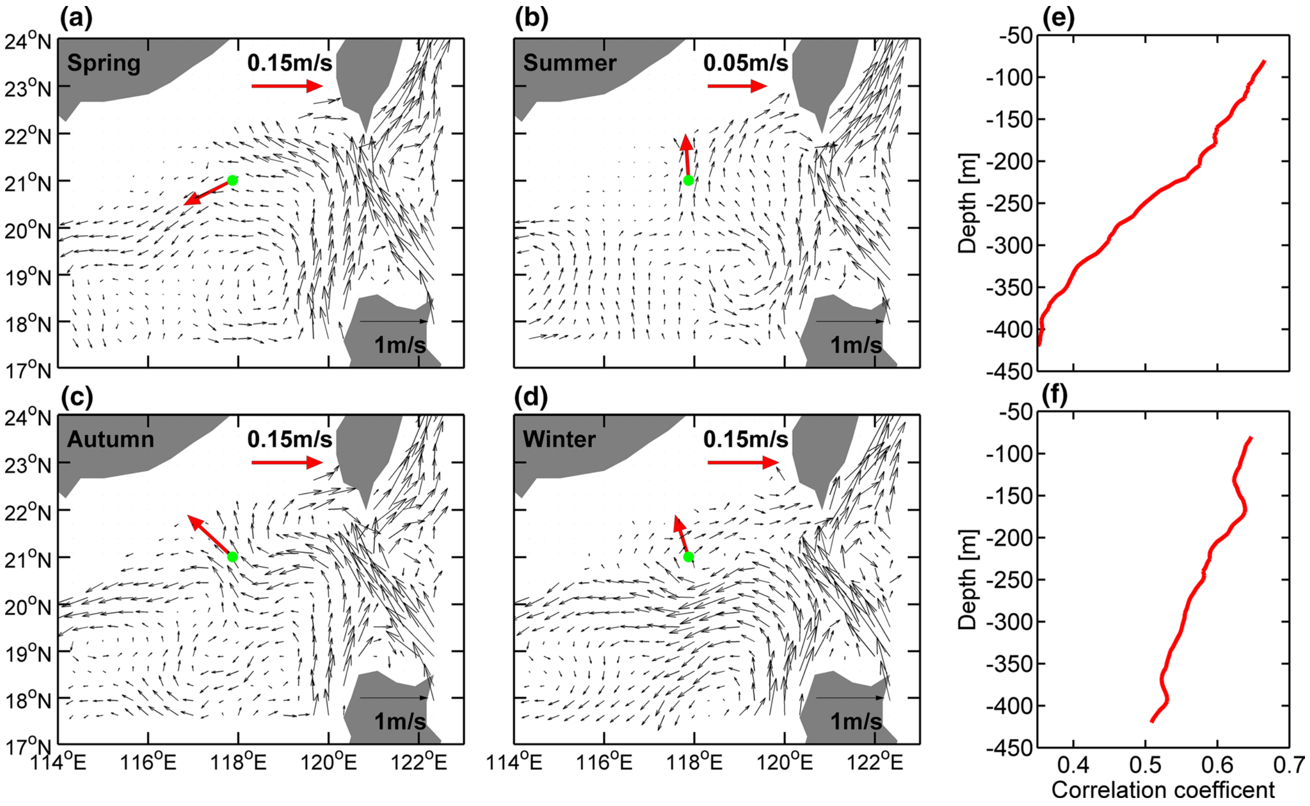

Fig. 4 **a** The mean altimeter geostrophic currents (*black arrows*) in the NSCS in springs of the whole mooring observation period. The currents in regions shallower than 200 m were not shown. The *green dot* is the mooring site, and the *red arrow* at the mooring site denotes the corresponding mooring-observed velocity at the uppermost common depth (80 m). **b**, **c** and **d** are the same as **a**, but for the summer, autumn and winter seasons, respectively. **e** *Vertical* profile of correlation coefficient between the mooring-observed *U* and the altimeter zonal geostrophic current (20.77°N–21.08°N and 117.67°E–118.0°E around the mooring site, satellite data). The correlation coefficients at each layer were all statistically significant above the 95 % confidence level. **f** is the same as **e**, but shows the result of the meridional velocity

Figs. 5a, b and Fig. 6a, we found that the observed large velocity anomalies and kinetic energy had a good correspondence with the eddy events. The observed largest kinetic energy in mid January was just corresponding to the strong mesoscale eddy WD, which showed a large SLA and SLA gradient (Figs. 6a, 7d). These results indicated that the eddies indeed had large influences on the local currents at the mooring site.

We assumed that the mooring site was influenced by the eddies only when it was at the edges or within the cores of eddies. If we defined the periods when mooring was influenced by the eddies as eddy periods, the eddy periods were 22 days (CA), 62 days (WB), 46 days (WC), 55 days (WD), 32 days (CE) and 40 days (WF), respectively (see Table 2). During the eddy periods, the detected eddies can cause a maximum absolute velocity of 0.62, 0.59, 0.21, 0.95, 0.35 and 0.71 m/s in the uppermost layer, respectively (see Table 2). The distance-time plots of the SLA along the latitude and longitude of the mooring site revealed propagating signals during the eddy events. Overall, WB and WC propagated northwestward, and the other four propagated southwestward. The propagation speed ranged from 6.8 to 9.3 cm/s (see Table 2), which generally agreed with the results of previous studies (Chen et al. 2011; Nan et al. 2011b). Figure 7 exhibits the typical SLA distribution when each detected eddy caused the maximum observed velocity during its eddy period. We found that, in nearly in all of the cases, the observed velocity reached its maximum mostly when the mooring site was at the edge of the eddies. In Fig. 7 we also show the generation locations and propagation trajectories of the eddies. Among the six eddies, WB and WC were generated northwest of Luzon, and WD, CE and WF were generated southwest of Taiwan. These generation regions were consistent with the primary eddy generation regions revealed by the historical statistics (Wang et al. 2003; Chen et al. 2011). The paths of the southwestward-propagating eddies (WD, CE and WF) were generally along the isobaths, which satisfied the conservation of potential vorticity (Zhang et al. 2013).

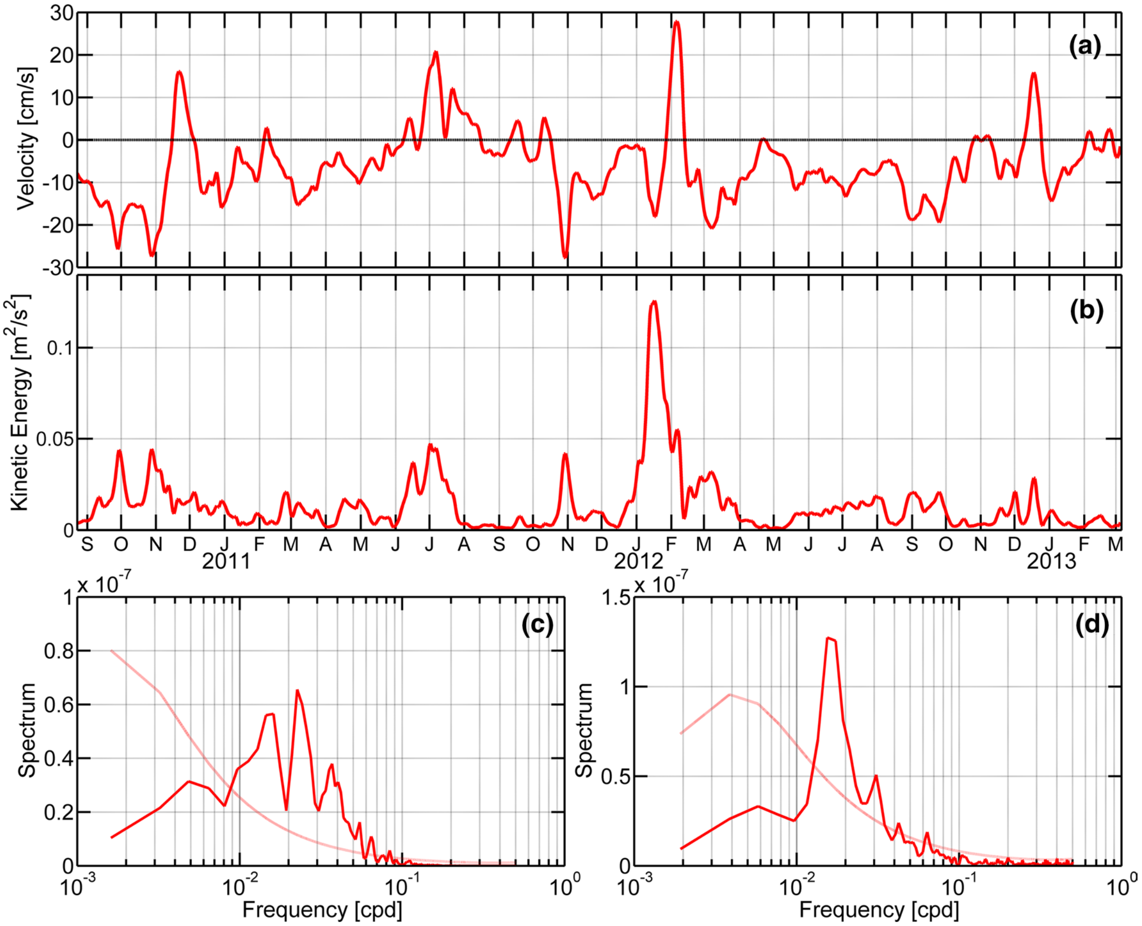

Fig. 5 **a** Time series of depth-averaged *U* between 80 and 420 m. **b** Time series of depth-averaged kinetic energy between 80 and 420 m. **c** The variance-preserved power spectrum of the depth-averaged *U* in **a**. The *red dashed line* indicates the 95 % confidence level. *Panel* **d** is the same as **c** but for the zonal altimeter geostrophic velocity (20.77°N–21.08°N and 117.67°E–118.0°E around the mooring site, satellite data)

To investigate the vertical structures of the strong ISV signals that were associated with the eddies, the mean velocity profile and its standard deviation were calculated during every eddy period (Fig. 8). For comparison, the mean profiles of the background current represented by 90-day low-passing velocity were also plotted. As the results for *U* and *V* were similar, we only showed the results of *V* here. During most eddy events, the mean *V* was apparently larger than the background *V*, demonstrating the influence of eddies on the local current. The velocity during all eddy periods had large variations and thus showed large standard deviations. The varying velocities during eddy periods were primarily caused by the propagation of eddies. During the whole observation period, different eddies presented different vertical structures. For the eddies CA, WB, WD and WF, the velocity was surface-intensified, i.e., with increasing depth the velocity quickly decreased. For eddies WC and CE, on the other hand, the velocity slightly increased with depth. Although the mean *V* had large vertical shears during eddy events, the mean *V* nearly keep the same sign in the vertical direction. Another interesting feature we should note was that during the WB, WC and WD periods the mean *V* was larger than the background velocity in the full water column; even beneath 800 m depth, the mean *V* can still have an order of 10 cm/s. This demonstrated that the mesoscale eddies are not only signals confined to the upper layer; sometimes they can extend from the sea surface to bottom.

To better understand the vertical structure of the observed current, the dynamical mode analysis was performed based on the near full-depth velocity data during the second observation period. We first computed the Brunt-Väisälä frequency from the WOA09 mean temperature and salinity profiles at the mooring site (Fig. 9a). Then the dynamical modes (Fig. 9b) were obtained by solving the Sturm-Liouville eigenvalue problem (Gill 1982). Referring to the method used in Wunsch (1997), the velocity profiles were projected onto each dynamical mode, and

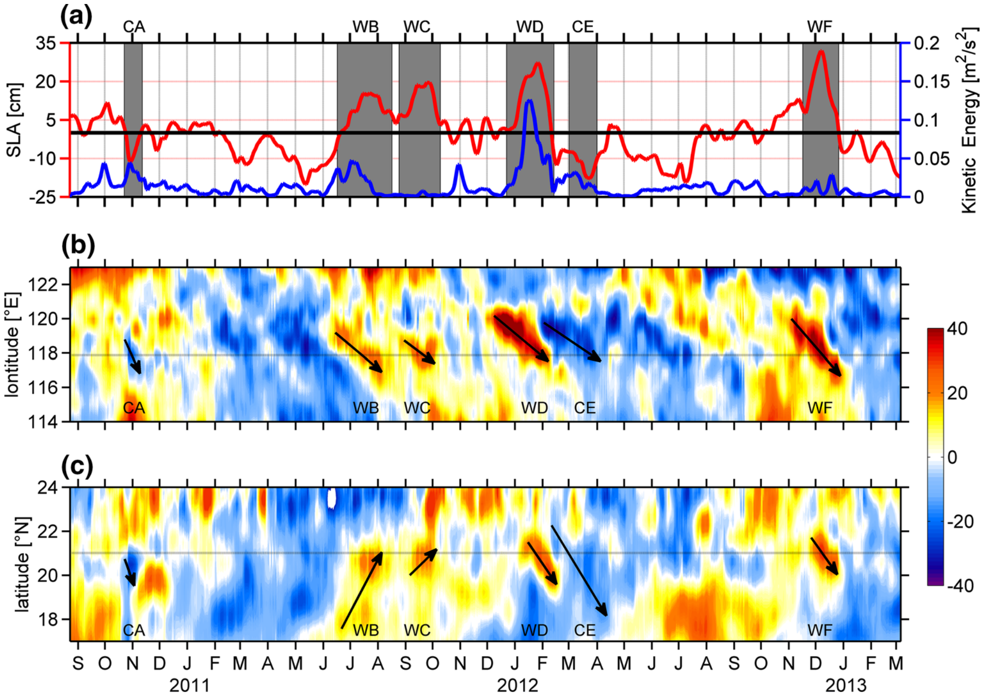

Fig. 6 **a** Time series of the altimeter SLA at the mooring site (*red line*) and the observed kinetic energy averaged over 80–420 m (*blue line*, same as Fig. 5b). The *gray strips* specify the mesoscale eddies passing the mooring site. Distance-time diagram of SLA along the longitude (**b**) and latitude (**c**) of the mooring site. The *black arrows* indicate the propagating eddy signals

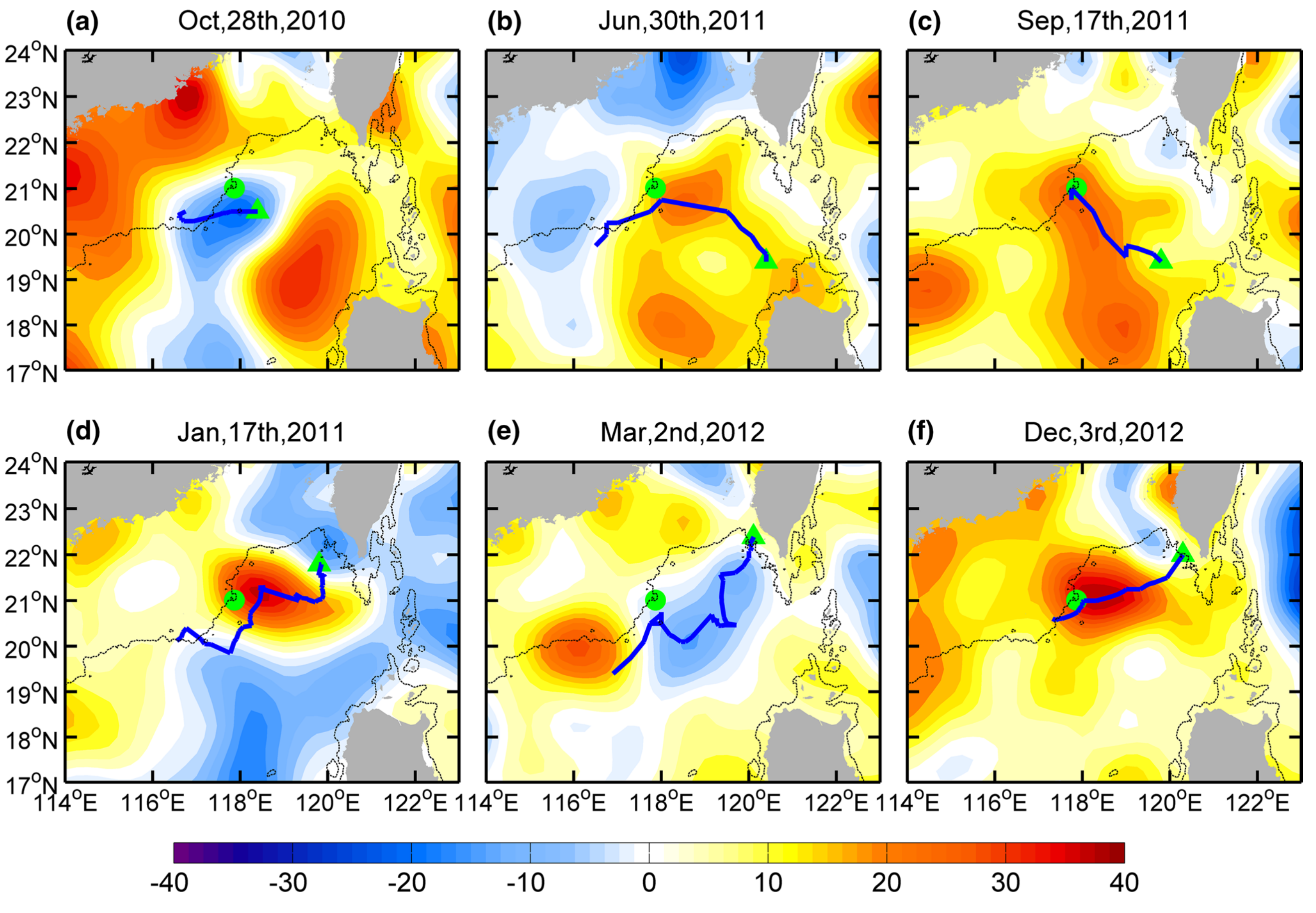

Fig. 7 The typical SLA distribution in the NSCS when each eddy revealed in Fig. 6a influenced the mooring site. The contour interval of SLA is 3 cm. The *black contour* denotes the 1000-m isobath. The *blue solid line* denotes the trajectory of each eddy. The *green dot* represents the mooring site, and the *triangle* represents the generation location of the eddy

Table 2 Statistics of the detected eddies

Eddy	Generation location	Generation time (year/month/day)	Propagation speed (cm/s)	Averaged SLA at mooring site during the eddy period (cm)	Eddy period (year/month/day)	Maximum observed velocity (m/s)	Time of the maximum velocity (year/month/day)
CA	118.4°E,20.5°N	10/10/17	8.6 ± 2.4	−5.0 ± 4.5	10/10/22–10/11/12	0.62	10/10/28
WB	120.4°E,19.4°N	11/5/10	9.3 ± 2.1	9.1 ± 5.5	11/6/17–11/8/17	0.59	11/6/30
WC	119.8°E,19.4°N	11/8/8	6.8 ± 1.6	12.6 ± 6.1	11/8/25–11/10/9	0.21	11/9/17
WD	119.75°E,21.75°N	11/11/26	7.9 ± 1.6	13.6 ± 10.7	11/12/21–12/2/13	0.95	12/1/17
CE	120°E,22.25°N	12/1/20	7.5 ± 1.8	−13.5 ± 4.1	12/3/1–12/4/1	0.35	12/3/2
WF	120.3°E,22°N	12/10/18	7.7 ± 1.4	17.6 ± 9.6	12/11/17–12/12/26	0.71	12/12/3

The statistics include mean values (to the left of the ± symbol) and standard deviations (to the right of the ± symbol)

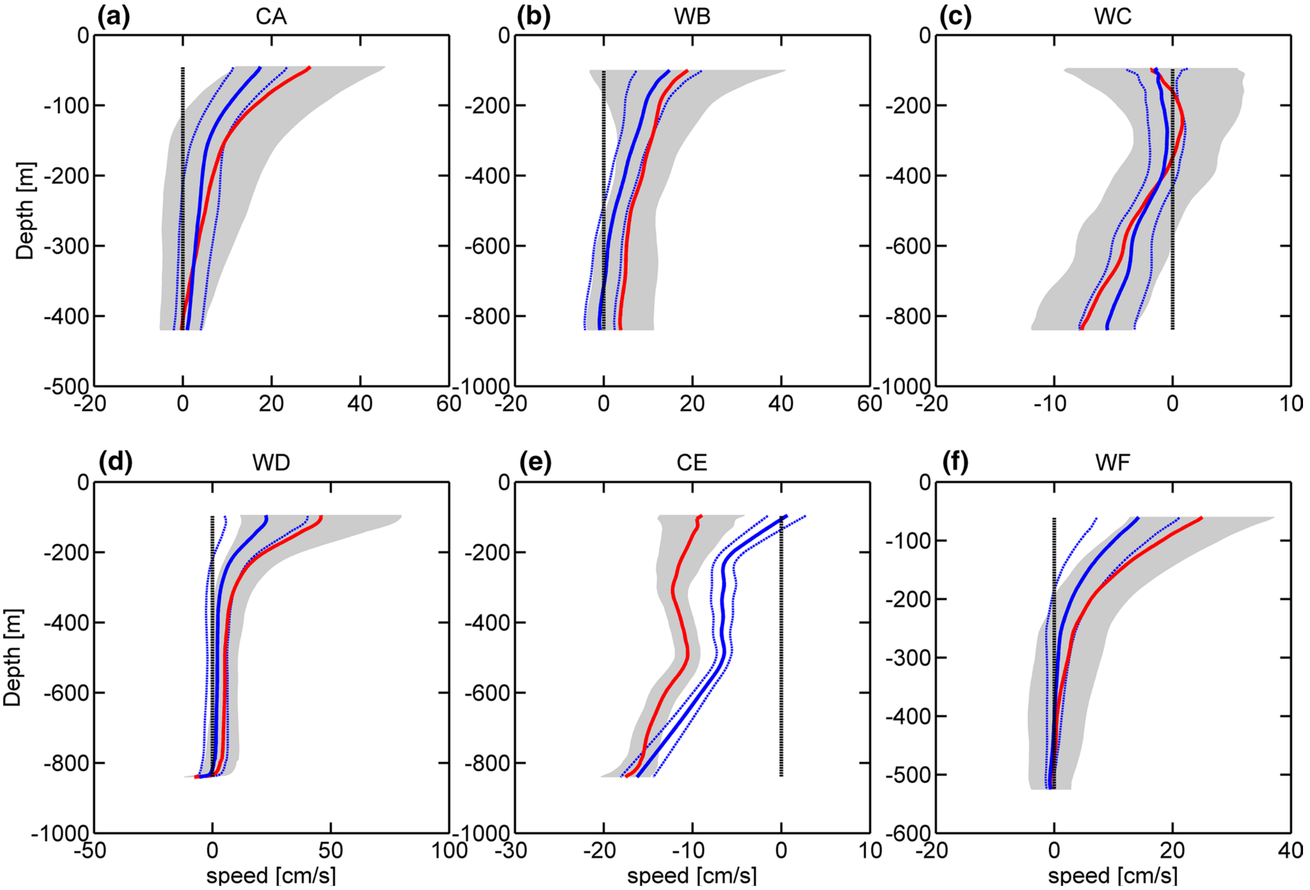

Fig. 8 **a** Time mean profile of *V* (*red line*) during the period when the mooring was influenced by eddy A. The *gray shading* denotes the standard deviation of the red line. The *blue solid line* is the same as the *red line* but was calculated from the 90-day low-pass filtered *V*. The *two blue dashed lines* denote the standard deviation of the *blue solid line*. The zero velocity is indicated by the *black dashed line*. *Panels* **b**–**f** are all the same as *panel* **a** except for the mean *V* profiles when the mooring was influenced by different eddies as marked on the *top of each panel*

the percentage of kinetic energy (KE) explained by each mode was calculated. The temporal variation of the result of the kinetic energy partition is shown in Fig. 9c. Because the energy explained by the high baroclinic mode (higher than 3) was weak, only the results of the barotropic and first three baroclinic modes were shown. The results show that the KE was concentrated in the barotropic mode during most of the observation period. The barotropic mode

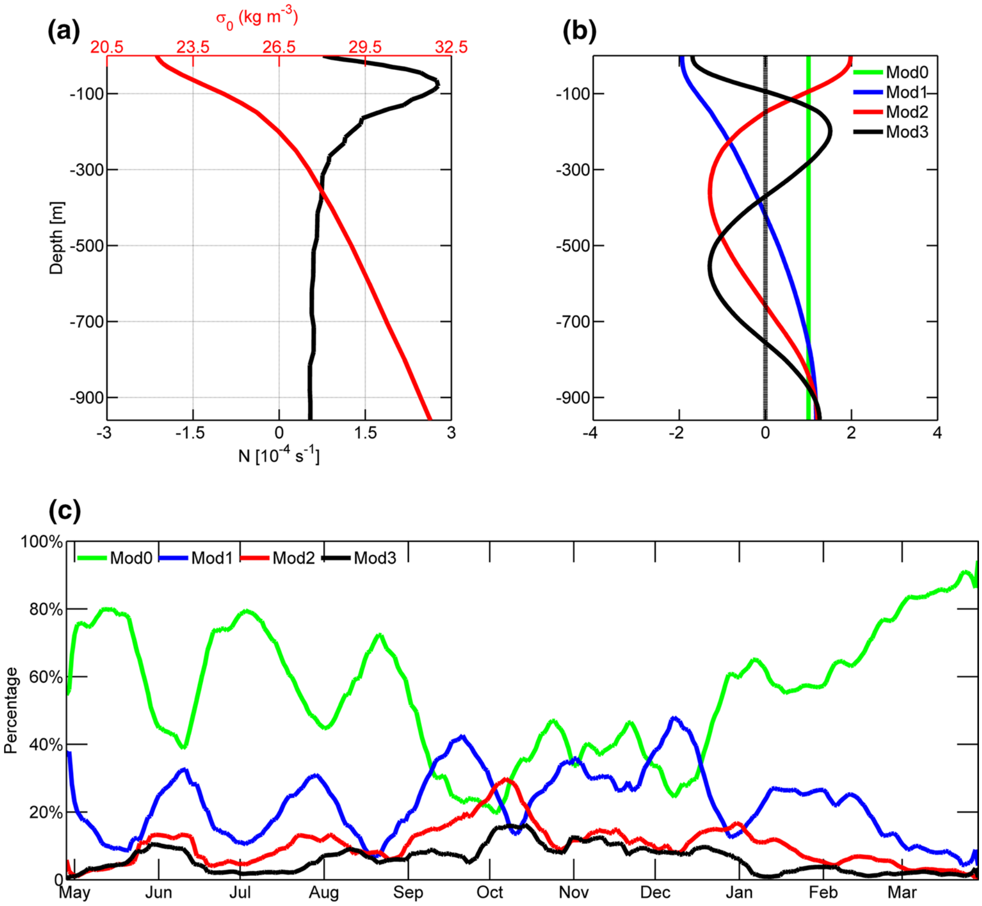

Fig. 9 **a** Mean potential density profile (*red*) and Brunt-Väisälä frequency (*black*). **b** The normalized barotropic (*mode 0*) and the first three baroclinic dynamical modes (*modes 1–3*). **c** The percentage of the full-column averaged kinetic energy in the barotropic and first three baroclinic modes

keeps the same velocity in the vertical direction (green line in Fig. 9b); the high barotropic mode energy explained why the observed currents were coherent and showed the same sign in the vertical direction (Fig. 2). However, in September and December, we found a relatively large energy percentage in the first baroclinic mode, which was comparable with the barotropic mode. During these two periods, the velocity showed large vertical shear as seen in Fig. 2. In addition, it was found that the mooring currents were influenced by a strong mesoscale eddy during both of the above two periods (Figs. 6, 7c, d). The above results indicated that the mesoscale eddy strengthened the vertical shear of the current velocity; thus, it had enhanced energy in the first baroclinic mode. Actually, the eddy structures were found to be dominated by the first baroclinic mode in the deep NSCS and Luzon Strait in our previous studies (Zhang et al. 2013, 2015).

4 Summary and discussion

The vertical structure and temporal variability of the current in the NSCS were examined based on 2.5-year direct velocity measurements from a subsurface mooring. Combining satellite altimeter and moored data, in this study we discussed the causes of the seasonal variability and ISVs of the mooring-observed currents.

Power spectrum analysis revealed that the observed velocity showed significant ISVs in the band between 30 and 90 days. The ISV-removed current velocity displayed a roughly semiannual cycle, with the depth-averaged U (V) reaching the maximum in March and October (January and July) and the minimum in July and February (April and August), respectively. Comparison with the altimeter observations suggested that this semiannual variability may be corresponding to the seasonally various circulation in the NSCS. In the previous studies (e.g., Qu et al. 2008, Kashino et al. 2011, Zhao et al. 2012), semiannual signals were also found in the upper-ocean circulation. Zhao et al. (2012) indicated that the semiannual signals in the northern Philippine Sea mainly resulted from semiannual modulations of the Asian Monsoon system. Since the NSCS is also under the control of the Asian Monsoon system, the semiannual variability of the current velocity may also be related to the Asian Monsoon. This needs further study in the future.

By combing the altimeter observations, it was found that the strong ISVs of the observed currents were closely related to the mesoscale eddies. During the whole observation period, we detected six long-lived eddies that influenced the mooring site for more than 20 days. One should note that several other eddies can also influence the mooring site and cause large velocity amplitudes (e.g., in late October 2011 and September 2012). As these eddies either were short-lived or only influenced the mooring site during a short period, we did not analyze them in the present study. Although we concluded in the present study that the propagating mesoscale eddies are an important cause of the ISVs of the observed current, the ISVs may also be associated with other factors, such as the propagating Rossby waves, some kinds of topography-trapped waves and intraseasonal sea surface wind forcing (Zhuang et al. 2010; Hsin et al. 2010).

The comparison between the mean velocity and background current profiles during eddy periods indicated that the mesoscale eddies are only not signals confined to the upper layer and that they sometimes can extend from the sea surface to bottom. The dynamical mode analysis of the near full-depth velocity data in the second deployment showed that the KE was concentrated in the barotropic mode during most of the observation period, which explained why the observed currents were coherent and showed the same sign in the vertical direction (Fig. 2). More importantly, the observations revealed that the mesoscale eddy can strengthen the vertical shear of the currents, which was also found by Chen et al. (2013). Correspondingly, the energy in the first baroclinic mode was enhanced during the eddy events. The altimeter SLA also indicated that the mooring was under the influence of a cold eddy in early December 2011 (not shown). Then, in mid and late December, the mooring was influenced by the WD. The velocity associated with these eddies had strong vertical shear; therefore the baroclinic energy was large in December 2011. We should note that the present result regarding the eddy vertical structure is only based on the observation from one mooring. The eddy may have different vertical structures in different regions and during its different life stages. This issue is left for the future study when more mooring observations will be acquired.

Our recent study indicated that the anti-cyclonic eddy generated southwest of Taiwan in December 2011 (eddy WD in the present study) was highly dominated by the first baroclinic mode in the deep basin; during the eddy event, the deep current below 2500 m was largely enhanced and showed opposite signs to the upper current (Zhang et al.2013). However, whether the mesoscale eddies can influence the basin-scale deep circulation in the SCS needs more full-depth observations for verification.

Acknowledgments We thank two anonymous reviewers for their helpful comments. This work was supported by the National Key Basic Research Program of China (Program 973; grant no. 2014CB745003), the National Key Scientific Research Project “the South China Sea Deep” (grant no. 91028008), the National Natural Science Foundation of China (grant no. 41176010, 41176008), the "Strategic Priority Research Program" of the Chinese Academy of Sciences (grant no. XDA11010202) and a grant from the Sanya Institute of Deep-Sea Science and Engineering (grant no. SIDSSE-201207).

References

Chen GX, Xue HJ (2014) Westward intensification in marginal seas. Ocean Dyn 64(3):337–345

Chen GX, Hou YJ, Chu XQ (2011) Mesoscale eddies in the South China Sea: mean properties, spatiotemporal variability, and impact on thermohaline structure. J Geophys Res 116:C06018. doi:10.1029/2010JC006716

Chen GX, Xue HJ, Wang DX, Xie Q (2013) Observed near-inertial kinetic energy in the northwestern South China Sea. J Geophys Res: Oceans 118(10):4965–4977. doi:10.1002/jgrc.20371

Gan JP, Li H, Curchitser EN, Haidvogel DB (2006) Modeling South China Sea circulation: response to seasonal forcing regimes. J Geophys Res 111:C06034. doi:10.1029/2005JC003298

Gill AE (1982) Atmosphere-Ocean dynamics. Academic Press, San Diego, p 662

Hsin YC, Qu TD, Wu CR (2010) Intra-seasonal variation of the Kuroshio southeast of Taiwan and its possible forcing mechanism. Ocean Dyn 60:1293–1306. doi:10.1007/s10236-010-0294-2

Hu JY, Kawamura H, Hong HS, Qi YQ (2000) A review on the currents in the South China Sea: seasonal circulation, South China Sea Warm Current and Kuroshio intrusion. J Oceanogr 56:607–624. doi:10.1023/A:1011117531252

Hu JY, Gan JP, Sun ZY, Zhu J, Dai MH (2011) Observed three-dimensional structure of a cold eddy in the southwestern South China Sea. J Geophys Res 116:C05016. doi:10.1029/2010JC006810

Hu JY, Zheng QA, Sun ZY, Tai CK (2012) Penetration of nonlinear Rossby eddies into South China Seaevidenced by cruise data. J Geophys Res 117:C03010. doi:10.1029/2011JC007525

Jia YL, Chassignet EP (2011) Seasonal variation of eddy shedding from the Kuroshio intrusion in the Luzon Strait. J Oceanogr 67:601–611

Kashino Y, Ishida A, Hosoda S (2011) Observed Ocean variability in the Mindanao Dome region. J Phys Oceanogr 41:287–302. doi:10.1175/2010JPO4329.1

Lan J, Zhang NN, Wang Y (2013) On the dynamics of the South China Sea deep circulation. J Geophys Res: Oceans 118(3):1206–1210. doi:10.1002/jgrc.20104

Liu WT, Xie X (1999) Space-based observations of the seasonal changes of South Asian monsoons and oceanic response. Geophys Res Lett 26:1473–1476. doi:10.1029/1999GL900289

Liu WT, Tang W, Xie X (2008) Wind power distribution over the ocean. Geophys Res Lett 35:L13808. doi:10.1029/2008GL034172

Maximenko N, Niiler P, Rio M, Melnichenko O, Centurioni L, Chambers D, Zlotnicki V, Galperin B (2009) Mean dynamic topography of the ocean derived from satellite and drifting buoy data using three different techniques. J Atmos Oceanic Tech 26(9):1910–1919

Morimoto A, Yoshimoto K, Yanagi T (2000) Characteristics of sea surface circulation and eddy field in the South China Sea revealed by satellite altimetric data. J Oceanogr 56(3):331–344

Nan F, He ZG, Zhou H, Wang DX (2011a) Three long-lived anticyclonic eddies in the northern South China Sea. J Geophys Res 116:C05002. doi:10.1029/2010JC006790

Nan F, Xue HJ, Xiu P, Chai P, Shi MC, Guo PF (2011b) Oceanic eddy formation and propagation southwest of Taiwan. J Geophys Res 116:C12045. doi:10.1029/2011JC007386

Nan F, Xue HJ, Chai F, Shi L, Shi MC, Guo PF (2011c) Identification of different types of Kuroshio intrusion into the South China Sea. Ocean Dyn 61:1291–1304. doi:10.1007/s10236-011-0426-3

Qu TD (2000) Upper-layer circulation in the South China Sea. J Phys Oceanogr 30(6):1450–1460. doi:10.1175/1520-0485(2000)030<1450:ULCITS>2.0.CO;2

Qu TD, Gan JP, Ishida A, Kashino Y, Tozuka T (2008) Semiannual variation in the western tropical Pacific Ocean. Geophys Res Lett 35:L16602. doi:10.1029/2008GL035058

Shaw PT (1991) The seasonal variation of the intrusion of the Philippine sea water into the South China Sea. J Geophys Res 96(C1):821–827. doi:10.1029/90JC02367

Shaw PT, Chao SY, Fu LL (1999) Sea surface height variations in the South China Sea from satellite altimetery. Oceanol Acta 22:1–17

Wang GH, Su JL, Chu PC (2003) Mesoscale eddies in the South China Sea observed with altimeter data. Geophys Res Lett 30(21):2121. doi:10.1029/2003GL018532

Wang DX, Xu HZ, Lin J, Hu JY (2008a) Anticyclonic eddies in the northeastern South China Sea during winter 2003/2004. J Oceanogr 64:925–935. doi:10.1007/s10872-008-0076-3

Wang GH, Chen D, Su J (2008b) Winter eddy genesis in the Eastern South China Sea due to Orographic wind jets. J Phys Oceanogr 38:726–732. doi:10.1175/2007JPO3868.1

Wang DX, Wang Q, Zhou WD, Cai SQ, Li L, Hong B (2013) An analysis of the current deflection around Dongsha Islands in the northern South China Sea. J Geophys Res: Oceans 118(1):490–501. doi:10.1029/2012JC008429

Wu CR, Chang CWJ (2005) Interannual variability of the South China Sea in a data assimilation model. Geophys Res Lett 32:L17611. doi:10.1029/2005GL023798

Wu CR, Chiang TL (2007) Mesoscale eddies in the northern South China Sea. Deep Sea Res Part II 54:1575–1588. doi:10.1016/j.dsr2.2007.05.008

Wu CR, Shaw PT, Chao SY (1998) Seasonal and interannual variations in the velocity field of the South China Sea. J Oceanogr 54(4):361–372

Wu CR, Tang TY, Lin SF (2005) Intra-seasonal variation in the velocity field of the northeastern South China Sea. Cont Shelf Res 25:2075–2083

Wunsch C (1997) The vertical partition of oceanic horizontal kinetic energy. J Phys Oceanogr 27:1770–1794

Wyrtki K (1961) Scientific results of marine investigations of the South China Sea and the Gulf of Thailand 1959–1961. NAGA report 2

Xiu P, Chai F, Shi L, Xue HJ, Chao Y (2010) A census of eddy activities in the South China Sea during 1993–2007. J Geophys Res 115:C03012. doi:10.1029/2009JC005657

Xu XZ, Qiu Z, Chen HC (1982) The general descriptions of the horizontal circulation in the South China Sea. In: Proceedings of the 1980 symposium on hydrometeology of the Chinese Society of oceanology and limnology, pp 137–141

Xue HJ, Chai F, Pettigrew N, Xu DY, Shi MC, Xu JP (2004) Kuroshio intrusion and the circulation in the South China Sea. J Geophys Res 109:C02017. doi:10.1029/2002JC001724

Zhang ZW, Zhao W, Tian JW, Liang XF (2013) A mesoscale eddy pair southwest of Taiwan and its influence on deep circulation. J Geophys Res Oceans. doi:10.1002/2013JC008994

Zhang ZW, Zhao W, Tian JW, Yang QX, Qu TD (2015) Spatial structure and temporal variability of the zonal flow in the Luzon Strait. J Geophys Res Oceans. doi:10.1002/2014JC010308

Zhao J, Li YL, Wang F, Zhai FG, Yu XL (2012) Spatial–temporal patterns and driving mechanisms of semiannual variations in the Philippine Sea. Deep Sea Res Part I 68:105–115

Zhuang W, Xie SP, Wang DX, Taguchi B, Aiki H, Sasaki H (2010) Intraseasonal variability in sea surface height over the South China Sea. J Geophys Res 115:C04010. doi:10.1029/2009JC005647